Polarity mechanisms such as contact inhibition of locomotion regulate persistent rotational motion of mammalian cells on micropatterns: SI Text

Brian A. Camley Yunsong Zhang Yanxiang Zhao Bo Li Eshel Ben-Jacob
Herbert Levine Wouter-Jan Rappel

1 Elements of the model and figure interpretation

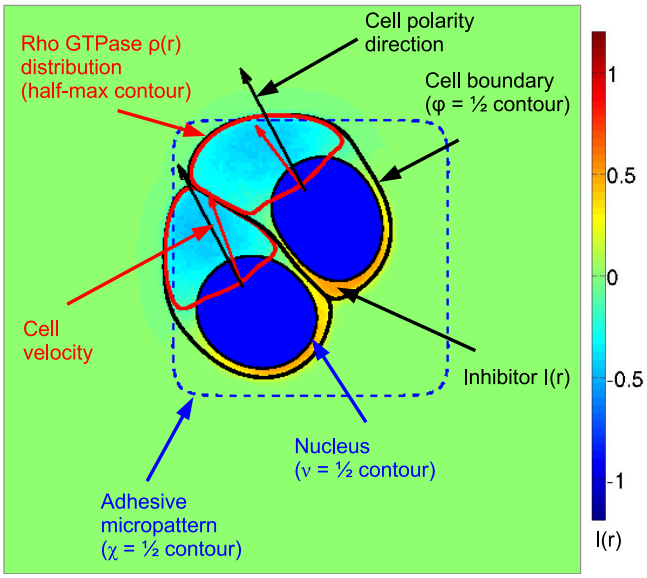

Figure S1: **Elements of model.** We track our cell's shape by a phase field $\phi(\mathbf{r})$; its boundary is plotted as a black line at the $\phi(\mathbf{r}) = 1/2$ contour. To show the cell front, where the Rho GTPase $\rho(\mathbf{r})$ is high, we plot the half-maximum contour of $\rho\phi$ in red. We show the nucleus in solid blue (its boundary is set by $\nu(\mathbf{r}) = 1/2$). The fluctuating inhibitor field $I(\mathbf{r})$ is shown as a color map ($I(\mathbf{r})\phi(\mathbf{r})$ is plotted to restrict I to the interior of the cell), with the color scale indicated to the right; all of our figures use this color scale for $I(\mathbf{r})$. We have also indicated the adhesive micropattern region; this is static, but indicated by a field $\chi(\mathbf{r})$. In some of our simulations, we will include an internal polarity vector for each cell, which will be plotted as a black vector. We have also plotted here the cell's center of mass velocity as a red vector.

2 Derivation of phase field equations from force balance

We briefly review the phase field method of tracking a cell boundary as developed in [1]. We assume that the cell interface motion is local and overdamped, i.e. that the interface velocity is directly proportional to the force applied to the interface:

$$\mathbf{v}_{\text{int}} = \frac{1}{\tau}\mathbf{F}_{\text{int}} \tag{S1}$$

where τ describes the frictional drag between the cell and substrate. The force $\mathbf{F}_{\text{int}}$ is the force per unit length. This is the same as arguing that the interface force is balanced by a frictional drag $\mathbf{F}_{\text{drag}} = -\tau\mathbf{v}_{\text{int}}$, with $\mathbf{F}_{\text{int}} + \mathbf{F}_{\text{drag}} = 0$. The boundary of the cell is tracked by a phase field $\phi(\mathbf{r}, t)$, which smoothly approaches zero outside the cell and approaches unity within it; the cell boundary is set implicitly by $\phi = 1/2$. We track the interface using the advection scheme:

$$\partial_t\phi + \mathbf{v}_{\text{int}} \cdot \nabla\phi = 0. \tag{S2}$$

The cell motion will depend on the origins of the force $\mathbf{F}_{\text{int}}$. In Shao et al. [1] there are three components to the force: 1) membrane tension and bending forces, derived from a Hamiltonian, 2) active forces arising from actin-based protrusion

and myosin-based contraction, and 3) a constraint force keeping the cell area fixed, $\mathbf{F}_{\rm int} = \mathbf{F}_{\rm H} + \mathbf{F}_{\rm active} + \mathbf{F}_{\rm area}$. Since we are including the possibility of cell spreading, we will not keep the cell area fixed in this work, though we will use a similar force to keep the cell's nuclear area constant. In addition, we will include terms in the Hamiltonian beyond the membrane deformations, including cell-cell adhesion and exclusion. We will not need to specify the Hamiltonian to derive the phase-field equations.

If $\phi(\mathbf{r})$ is not given by the energy-minimizing state $\frac{\delta H}{\delta \phi} = 0$, we can write down the induced force density [2,3]

$$\mathbf{F}^*_{\rm H}(\mathbf{r}) = \frac{\delta H}{\delta \phi} \nabla \phi. \tag{S3}$$

To convert between a two-dimensional force density $\mathbf{F}^*$ and its corresponding interfacial force $\mathbf{F}$ as used in Eq.S1, we use a function $\delta_\epsilon(\mathbf{r}) = \epsilon |\nabla \phi|^2$ which indicates the interface. We then write

$$\mathbf{F}^* d^2 r = \mathbf{F} d\ell = \mathbf{F} \delta_\epsilon(\mathbf{r}) d^2 r \tag{S4}$$

e.g. $\mathbf{F}_{\rm H} = \mathbf{F}^*_{\rm H}/\delta_\epsilon(\mathbf{r})$.

We use a simple form for the active forces at the membrane's surface, setting (in the absence of any micropattern)

$$\mathbf{F}_{\rm active} = (\alpha \rho - \beta)\, \hat{\mathbf{n}} \tag{S5}$$

where ρ is the concentration of actin promoter within the cell and $\hat{\mathbf{n}} = -\frac{\nabla \phi}{|\nabla \phi|}$ is the outward-pointing normal to the cell surface. Similar choices are used in [1,4]. Under this minimal rule, the area of the cell where ρ is high will be pushed outward, and the back of the cell where ρ is low (smaller than β/α) will be pulled in.

Combining these results, we can write $\mathbf{v}_{\rm int}$ in terms of the fields ϕ and ρ, and our equation of motion for $\phi(\mathbf{r}, t)$ (Eq.S2) becomes

$$\partial_t \phi(\mathbf{r}, t) = \frac{1}{\tau} (\alpha \rho - \beta) |\nabla \phi| - \frac{1}{\tau \epsilon} \frac{\delta H}{\delta \phi}. \tag{S6}$$

2.1 Inclusion of cell nucleus

We treat the cell nucleus using a second phase field, $\nu(\mathbf{r}, t)$. This nucleus is modeled as an object with a fixed line tension $\gamma_{\rm nuc}$ and bending modulus $\kappa_{\rm nuc}$, as well as an area constraint fixing its area to $A_{\rm nuc} = \pi R^2_{\rm nuc}$. We implement this area constraint as an isotropic penalty force, as in [1]

$$\mathbf{F}_{\rm area} = -M (A_\nu - A_{\rm nuc})\, \hat{\mathbf{n}}_\nu \tag{S7}$$

where $A_\nu = \int d^2 r \nu(\mathbf{r})$; M is a multiplier chosen to be large enough to keep the nuclear area roughly fixed, and $\hat{\mathbf{n}}_\nu = -\frac{\nabla \nu}{|\nabla \nu|}$ is the outward-pointing normal to the nucleus surface. The equation for the nucleus phase field $\nu(\mathbf{r}, t)$ becomes

$$\partial_t \nu(\mathbf{r}, t) = -\frac{M}{\tau_{\rm nuc}} (A_\nu - A_{\rm nuc}) |\nabla \nu| - \frac{1}{\tau_{\rm nuc} \epsilon} \frac{\delta H}{\delta \nu} \tag{S8}$$

where $\tau_{\rm nuc}$ is the nuclear equivalent of τ, a friction coefficient relating the velocity of the nucleus' boundary to the forces applied to it. We note that we have allowed $\tau_{\rm nuc}$ to differ from τ; this term reflects the friction on the nucleus. If $\tau_{\rm nuc}$ is increased, the cell will eventually be unable to pull the nucleus.

The generalization to many cells, which is presented explicitly in the main paper, is straightforward.

2.2 Effect of micropattern on cell dynamics

We model the micropattern with an approach similar to the one we used in [5]. We represent the micropattern by a normalized ligand density $\chi(\mathbf{r})$, and restrict protrusion to occur only on the micropattern, i.e. we set $\mathbf{F}_{\rm active} = [\alpha \chi(\mathbf{r}) \rho - \beta]\, \hat{\mathbf{n}}$. This models the cell as unable to generate pushing forces without the adhesion between the cell and substrate. We then have a phase field equation of the form

$$\partial_t \phi(\mathbf{r}, t) = \frac{1}{\tau} [\alpha \chi(\mathbf{r}) \rho(\mathbf{r}) - \beta] |\nabla \phi| - \frac{1}{\tau \epsilon} \frac{\delta H}{\delta \phi}. \tag{S9}$$

To model a smooth profile of ligand, we choose the form

$$\begin{aligned} \chi(\mathbf{r}) = \frac{1}{16} &\left[1 + \tanh\left(\frac{L_{\rm micro}/2 - x}{\epsilon}\right)\right] \left[1 + \tanh\left(\frac{L_{\rm micro}/2 - y}{\epsilon}\right)\right] \times \\ &\left[1 + \tanh\left(\frac{x + L_{\rm micro}/2}{\epsilon}\right)\right] \left[1 + \tanh\left(\frac{y + L_{\rm micro}/2}{\epsilon}\right)\right] \end{aligned} \tag{S10}$$

which describes an adhesive square of size $L_{\rm micro} \times L_{\rm micro}$. Other micropattern shapes can be very simply generated by choosing a different form for $\chi(\mathbf{r})$; we show an example of cell dynamics on a circular micropattern in Fig.S5.

3 Reaction-diffusion mechanisms within the cell: reaction terms f_ρ and f_I

3.1 $\rho(\mathbf{r})$ dynamics: cell front-back polarity

We describe the dynamics of the cell's chemical polarization using a variant of the reaction-diffusion model first proposed by Mori et al. [6]. This model describes the dynamics of a Rho GTPase that defines the front front of the cell, e.g. Rac or cdc42. In this model, the Rho GTPase may move between membrane-bound ($\rho(\mathbf{r},t)$) and cytosolic ($\rho_{\rm cyt}$) states. The membrane-bound state recruits ρ from the cytoplasm, but the total number $N_{\rm tot}$ of Rho GTPase molecules is conserved. We assume that the cytoplasmic Rho GTPase $\rho_{\rm cyt}$ is well-mixed (i.e. constant) over the time scales studied, while ρ diffuses with a diffusion coefficient D_ρ. This model robustly produces a well-defined "front" (high ρ) and "back" (low ρ) to the cell.

This reaction-diffusion model has a reaction term $f_\rho(\rho,\rho_{\rm cyt},I)$ where

$$f_\rho(\rho,\rho_{\rm cyt},I) = k_b\left(\frac{\rho^2}{K_a^2+\rho^2}+k_a\right)\rho_{\rm cyt} - k_c\left[1+I(\mathbf{r})\right]\rho. \tag{S11}$$

As described above, this reaction term includes a transition from membrane-bound to cytosolic state with reaction rate constant $k_c(1+I)$ (i.e. positive I increases the rate of transition $\rho\to\rho_{\rm cyt}$), a first-order rate from cytosolic to membrane-bound ($k_a k_b$), and a nonlinear term describing recruitment. The total amount of ρ is conserved, $\int d^2r\,(\rho(\mathbf{r})+\rho_{\rm cyt})\,\phi(\mathbf{r}) = N_{\rm tot}$. We assume that the cytosolic actin promoter is well-mixed (uniform), so $\rho_{\rm cyt}$ is "slaved" to ρ:

$$\rho_{\rm cyt} = \frac{N_{\rm tot} - \int d^2r\rho(\mathbf{r})\phi(\mathbf{r})}{\int d^2r\phi(\mathbf{r})}. \tag{S12}$$

3.2 $I(\mathbf{r})$ dynamics: calibrating persistence of single model cells

As discussed in the main text, we introduce a fluctuating field $I(\mathbf{r})$ to control the cell's persistence, i.e. the time over which the cell's direction and velocity are maintained. We also use this field to describe polarity mechanisms. This field has a reaction term

$$f_I(I,\{\phi\}) = -k_{-I}I + \xi(\mathbf{r},t) + \text{polarity mechanism terms}. \tag{S13}$$

$\xi(\mathbf{r},t)$ is a Gaussian Langevin noise with zero mean and a variance

$$\langle\xi(\mathbf{r},t)\xi(\mathbf{r}',t')\rangle = \eta^2\delta^2(\mathbf{r}-\mathbf{r}')\delta(t-t'). \tag{S14}$$

In practice, when we numerically solve the reaction-diffusion equations, we will represent the Dirac delta function above as a Gaussian random variable that is uncorrelated between lattice sites, but with a variance rescaled by Δx^{-2}; this is required to ensure that the noise amplitude will not change if the resolution changes (numerical details in Section 13).

We note that earlier models exist for the description of cell protrusions and polarity; many of these are reviewed in [7–9]. We have chosen the mechanism here for its relative simplicity, and because it reduces easily to a steadily-crawling model in the limit $\eta\to 0$.

We systematically vary the noise strength η and measure its effect on the center of mass motion of the cell (Fig.S2). As the units of η^2 are $\mu m^2/s$, we will instead report $\bar\eta^2 = \eta^2/D_I$, which is unitless. We measure the velocity-velocity correlation of the cell center of mass, $\mathbf{R}_{\rm cm}$,

$$\mathbf{R}_{\rm cm} \equiv \frac{\int d^2r\ \mathbf{r}\,\phi(\mathbf{r})}{\int\ d^2r\phi(\mathbf{r})} \tag{S15}$$

and $\mathbf{v}_{\rm cm} = \frac{d}{dt}\mathbf{R}_{\rm cm}$. We define $t_{1/2}$ as the time at which the relevant normalized velocity-velocity correlation function reaches 1/2, i.e.

$$C_{vv}(t_{1/2}) = \frac{\langle\mathbf{v}_{\rm cm}(t+t_{1/2})\cdot\mathbf{v}_{\rm cm}(t)\rangle}{\langle|\mathbf{v}_{\rm cm}|^2\rangle} = \frac{1}{2}. \tag{S16}$$

We find that the persistence time $t_{1/2}$ of the cell center of mass increase sharply as $\bar\eta$ is decreased to zero (Fig.S2). These results are for the reaction term above, with no polarity mechanism assumed; if a VA or NA mechanism is applied, this may potentially change the cell persistence.

4 The cell-cell adhesion force: what does σ mean?

The cell-cell adhesion term is given by

$$H_{\rm adhesion} = -\sum_{i\neq j}\int d^2r\frac{\sigma\epsilon^3}{4}|\nabla\phi^{(i)}|^2|\nabla\phi^{(j)}|^2. \tag{S17}$$

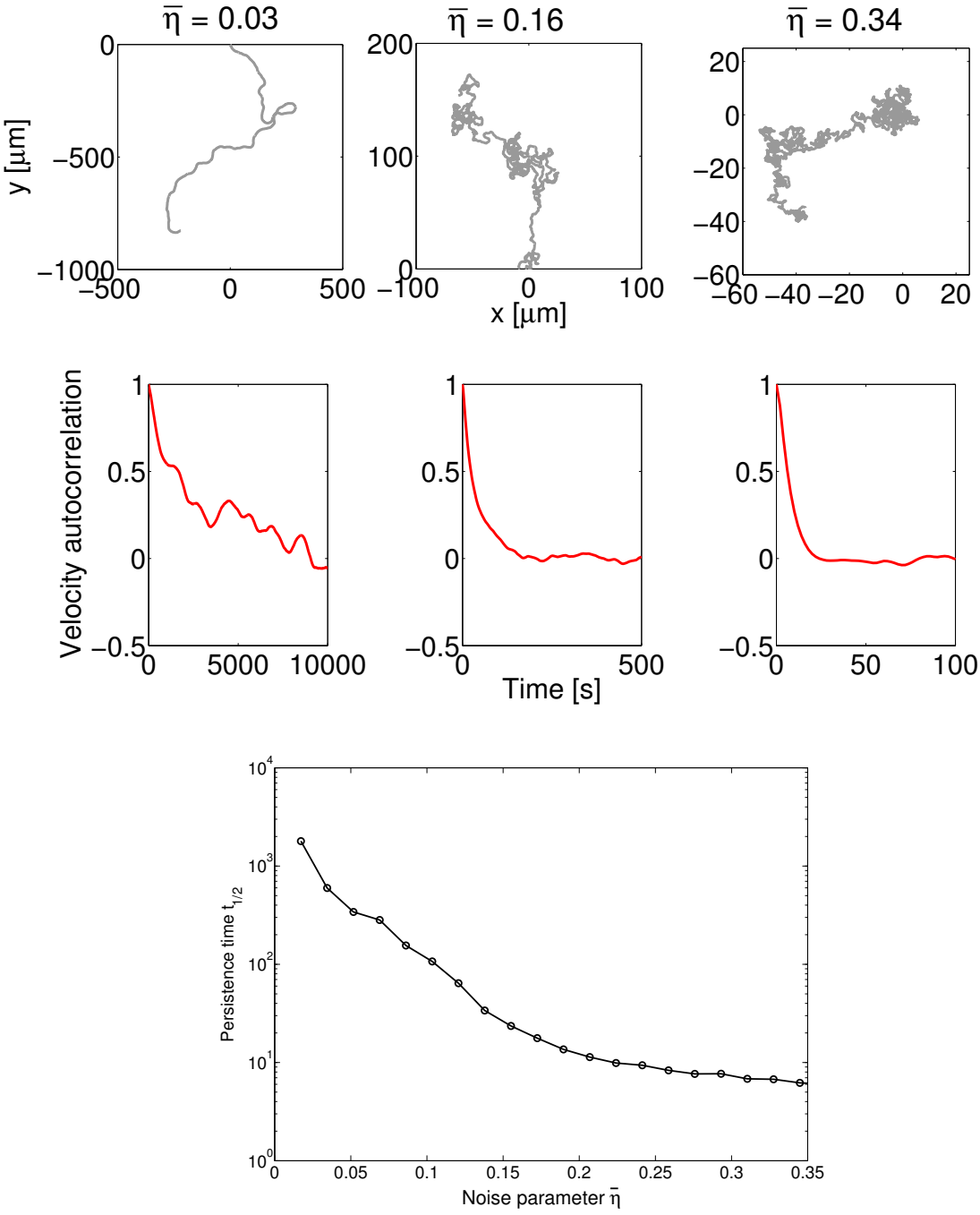

Figure S2: **Changing inhibitor noise $\bar{\eta}$ changes cell persistence.** We show how single-cell trajectories (first row) and normalized velocity autocorrelation functions (second row) change as a function of the inhibitor noise $\bar{\eta}$ (where $\bar{\eta}^2 = \eta^2/D_I$). We can characterize this general behavior by looking at the persistence time $t_{1/2}$. We define $t_{1/2}$ as the time at which the normalized velocity-velocity correlation function reaches 1/2, i.e. $\langle \mathbf{v}(t + t_{1/2}) \cdot \mathbf{v}(t) \rangle = \frac{1}{2}\langle |\mathbf{v}|^2 \rangle$. These single-cell simulations are performed with a larger time step of $\Delta t = 0.005$. Trajectories are plotted for times of 20,000 seconds, 20,000 seconds, and 15,000 seconds for $\bar{\eta} = 0.03, 0.16$, and 0.34 respectively; this is also the data used to create the velocity-velocity autocorrelations.

The sum $\sum_{i\neq j}$ is a sum over i and j from 1 to n_c, excepting only $i = j$ – we note that each cell pair is counted twice in this sum in our convention. σ sets the scale of the energy of adhesion; it has units of energy per unit length. However, σ is not a numerically precise energy of adhesion per length of overlap. We consider two perfectly overlapping interfaces that minimize the Helfrich energy (H_ϕ), $\phi^{(1)} = \frac{1}{2}(1 + \tanh\frac{3x}{\epsilon})$ and $\phi^{(2)} = \frac{1}{2}(1 - \tanh\frac{3x}{\epsilon})$. For a fixed length L in the y direction, we find $H_{\text{adhesion}} = -\sigma L\frac{27}{32}\int_{-\infty}^{\infty} du\ \text{sech}^8 u = -\frac{27}{35}\sigma L$; the effective adhesion energy per overlapping length is $\frac{27}{35}\sigma \approx 0.77\sigma$. If the interfaces are curved, or otherwise distorted (e.g. by the cell-cell repulsion), this result may also be quantitatively altered.

4.1 A note on the sharp-interface limit

The quantitative application of phase field methods is often made more difficult by the need to reach a sharp interface limit, $\epsilon \to 0$ (see, e.g. Ref. [10] and references within). Because our focus in this work is not quantitative comparisons, we will not explicitly study this aspect. However, we should note that our approach (and the related one of Nonomura [11]) raise interesting questions about the sharp interface limit of the adhesion terms proposed phenomenologically here. In the limit $\epsilon \to 0$, what does Eq.S17 mean? Our simple argument above suggests that it corresponds to an energy of $-\frac{27}{35}\sigma$ per unit length of overlapping edge - but the meaning of "overlapping" in a sharp interface sense may not be clear.

Attempts to refine our calculations for $\epsilon \to 0$ would also need to address the sharp-interface limit of the cell-cell interactions in polarity mechanisms, as described in Section 6.

5 Initial conditions

In our multiple-cell simulations, we initiate the cells with different positions as well as different random initial distributions of $\rho(\mathbf{r})$. We choose the initial centers of the cells with a uniform distribution over the square micropattern $-L_{\text{micro}}/2 \leq x \leq L_{\text{micro}}/2, -L_{\text{micro}}/2 \leq y \leq L_{\text{micro}}/2$, excluding only those configurations where the cell centers are within $0.3R_{\text{cell}}$ of each other. This includes cases with some initial overlap - the cells quickly move and deform to eliminate this overlap. We choose an initial cell size of $R_{\text{cell}} = 10\ \mu m$, which we implement as an initial ϕ field $\phi(\mathbf{r}) = \frac{1}{2} + \frac{1}{2}\tanh[3(R_{\text{cell}} - r)/\epsilon]$, where r indicates the distance from the chosen center of mass. (An equivalent choice is made for the initial value of $\nu(\mathbf{r})$, but with the nuclear radius R_{nuc}). The ρ distribution is initialized to a uniform value with a large noise, leading the cells to spontaneously develop a polarity. This distribution for ρ is $\max(1.8 + \text{noise}, 0)\ \mu m^{-2}$ where the noise is normally-distributed at each lattice point with a standard deviation of $1.8\mu m^{-2}$. Initially, $I(\mathbf{r})$ is set to zero everywhere.

6 Implementing polarity mechanisms in a phase field model

We can use our combined mechanical and chemical model as a platform to implement several potential mechanisms to determine the in-plane polarity of our cells. These polarity mechanisms are contact inhibition of locomotion (CIL), front-front inhibition (FF), neighbor alignment (NA), and velocity alignment (VA).

6.1 Contact inhibition of locomotion (CIL)

To model contact inhibition of locomotion (CIL), we generate the inhibitor I in cells where they contact their neighbors; neighbor contact is indicated by the nonzero value of a phase field other than the cell's. We modify the reaction term f_I,

$$f_I^{\text{CIL}}[I^{(i)}, \{\phi\}] = k_I S\left(\sum_{j\neq i}\phi^{(j)}\right) - k_{-I}I^{(i)} + \xi^{(i)}(\mathbf{r}, t) \tag{S18}$$

where $S(x) = \max(0, \tanh[x/x_0])$. Here, k_I controls the strength of the generation of inhibitor, and the form of $S(x)$ is chosen to saturate, so that large overlaps between cells do not generate huge amounts of I; we choose $x_0 = 0.1$ throughout this paper.

6.2 Front-front inhibition (FF)

We generalize the idea of contact inhibition of locomotion to the case where only contact with the front of the cell (ρ large) leads to inhibition:

$$f_I^{\text{FF}}[I^{(i)}, \{\phi\}, \{\rho\}] = k_I S\left(\frac{\sum_{j\neq i}\rho^{(j)}\phi^{(j)}}{\rho^{\text{char}}}\right) - k_{-I}I^{(i)} + \xi^{(i)}(\mathbf{r}, t) \tag{S19}$$

where $S(x) = \max(0, \tanh[x/x_0])$, $x_0 = 0.1$ as above, and we set $\rho^{\text{char}} = 1\mu m^{-2}$. This characteristic scale is smaller than the typical value of ρ at the cell front, which is usually around $1.4\mu m^{-2}$, but is much larger than the value at the back, which is typically around $0.01\mu m^{-2}$.

6.3 Velocity-alignment of polarity (VA)

We introduce a unit vector for each cell to track the cell's targeted polarity, $\hat{\mathbf{p}}^{(i)} \equiv (\cos\theta^{(i)}, \sin\theta^{(i)})$. This additional polarity vector has its own dynamics. For the VA model, we follow [12–14] in aligning the polarity of the cell with its velocity. We write the dynamics of $\hat{\mathbf{p}}^{(i)}$ as

$$\partial_t \theta^{(i)} = \frac{1}{T_{\text{orient}}} \arcsin\left[\cos\theta^{(i)} \sin\theta_v^{(i)} - \sin\theta^{(i)} \cos\theta_v^{(i)}\right] + \zeta z(t) \tag{S20}$$

where $\theta_v^{(i)} = \arg \mathbf{v}_{\text{cm}}^{(i)}$ is the angle of the cell's center-of-mass velocity and $z(t)$ is a Gaussian Langevin noise with unit variance, $\langle z(t) z(t') \rangle = \delta(t - t')$. This form is the one suggested originally by Szabo et al. [12]; it is an appropriate periodic extension of writing $-\frac{1}{T_{\text{orient}}}\left(\theta^{(i)} - \theta_v\right)$ [15]. Note that $\arcsin\left[\cos\theta^{(i)} \sin\theta_v^{(i)} - \sin\theta^{(i)} \cos\theta_v^{(i)}\right] = \arcsin\left[-\sin\left(\theta^{(i)} - \theta_v^{(i)}\right)\right] = -\left(\theta^{(i)} - \theta_v^{(i)}\right)$, where the last equality holds when $|\theta^{(i)} - \theta_v^{(i)}| \leq \pi/2$.

In order to make the Rho GTPase align with our new polarity vector $\hat{\mathbf{p}}^{(i)}$, we modify the reaction kinetics of the inhibitor I:

$$f_I^{\text{pol}}[I^{(i)}, \{\phi\}] = -k_I \hat{\mathbf{p}}^{(i)} \cdot \left(\frac{\mathbf{r} - \mathbf{R}_{\text{cm}}^{(i)}}{|\mathbf{r} - \mathbf{R}_{\text{cm}}^{(i)}|}\right) - k_{-I} I^{(i)} + \xi^{(i)}(\mathbf{r}, t) \tag{S21}$$

where the center of mass of cell i is given by

$$\mathbf{R}_{\text{cm}}^{(i)} = \frac{\int d^2 r \mathbf{r} \phi^{(i)}(\mathbf{r})}{\int d^2 r \phi^{(i)}}. \tag{S22}$$

We note that though ζ is large and the polarity fluctuates strongly around the velocity, the orientational persistence time $t_{1/2}$ of a single VA cell (around 1300 seconds with default parameters) remains comparable to that of a single CIL or FF cell (around 1700 s); if ζ is set to zero, a VA cell has a significantly larger persistence time than a FF cell.

6.4 Neighbor-alignment of velocities (NA)

To model alignment between neighboring cells, we use the scheme from the previous section, including Eq.S21, but alter the dynamics of the polarity vector $\hat{\mathbf{p}}^{(i)}$. We choose, similarly to the VA model,

$$\partial_t \theta^{(i)} = \frac{1}{T_{\text{orient}}} \arcsin\left[\cos\theta^{(i)} \sin\theta_{\bar{v}} - \sin\theta^{(i)} \cos\theta_{\bar{v}}\right] + \zeta z(t) \tag{S23}$$

where $z(t)$ is a Langevin noise as above, $\theta_{\bar{v}} = \arg \bar{\mathbf{v}}_{\text{cm}}$, and $\bar{\mathbf{v}}_{\text{cm}}$ is the mean velocity of all cells in our system, where $\mathbf{v}_{\text{cm}}^{(i)} = \frac{d}{dt}\mathbf{R}_{\text{cm}}^{(i)}$. In simulations of larger collections of cells, a cutoff distance is usually applied for this alignment interaction [16]; in our model, we assume that this cutoff distance is larger than the micropattern.

7 Effect of polarity mechanisms in $L_{\text{micro}} = 30\ \mu m$ micropattern

We have shown typical simulations of PRM in micropatterns of size $L_{\text{micro}} = 25\ \mu m$ in the main paper. We compare these results to simulations in $L_{\text{micro}} = 30\ \mu m$ micropatterns in Fig.S3. The primary effect of increasing micropattern size is to disrupt PRM for FF cells.

8 Cell rotational motion is disrupted in cells with lower persistence

We have shown that the presence and robustness of persistent rotational motion can be controlled by polarity alignment mechanisms. However, persistent rotational motion also requires that the cell's linear motion be sufficiently persistent; as the model of Huang et al. [17] makes clear, cells that undergo effectively pure random-walk motility are not likely to develop rotation. In our model, the persistence time (as measured from the cell's velocity-velocity correlation function) is controlled by the amplitude of the fluctuating source term in the $I(\mathbf{r})$ equation (see Fig.S2). In Fig.S4, we vary this amplitude, $\bar{\eta}$, and show that the presence of persistent rotation is disrupted at large $\bar{\eta}$. The simulations presented in Fig.S4 use the FF mechanism in a 25 μm micropattern, which robustly generates PRM for highly persistent cells ($\bar{\eta} = 0.03$). Decreasing persistence can lead to transient reversals, as well as complete elimination of rotation in some cases. We do not perform a similar analysis for the velocity-alignment mechanism, as VA cells will have a different calibration between persistence time and the noise $\bar{\eta}$ and the noise strength ζ.

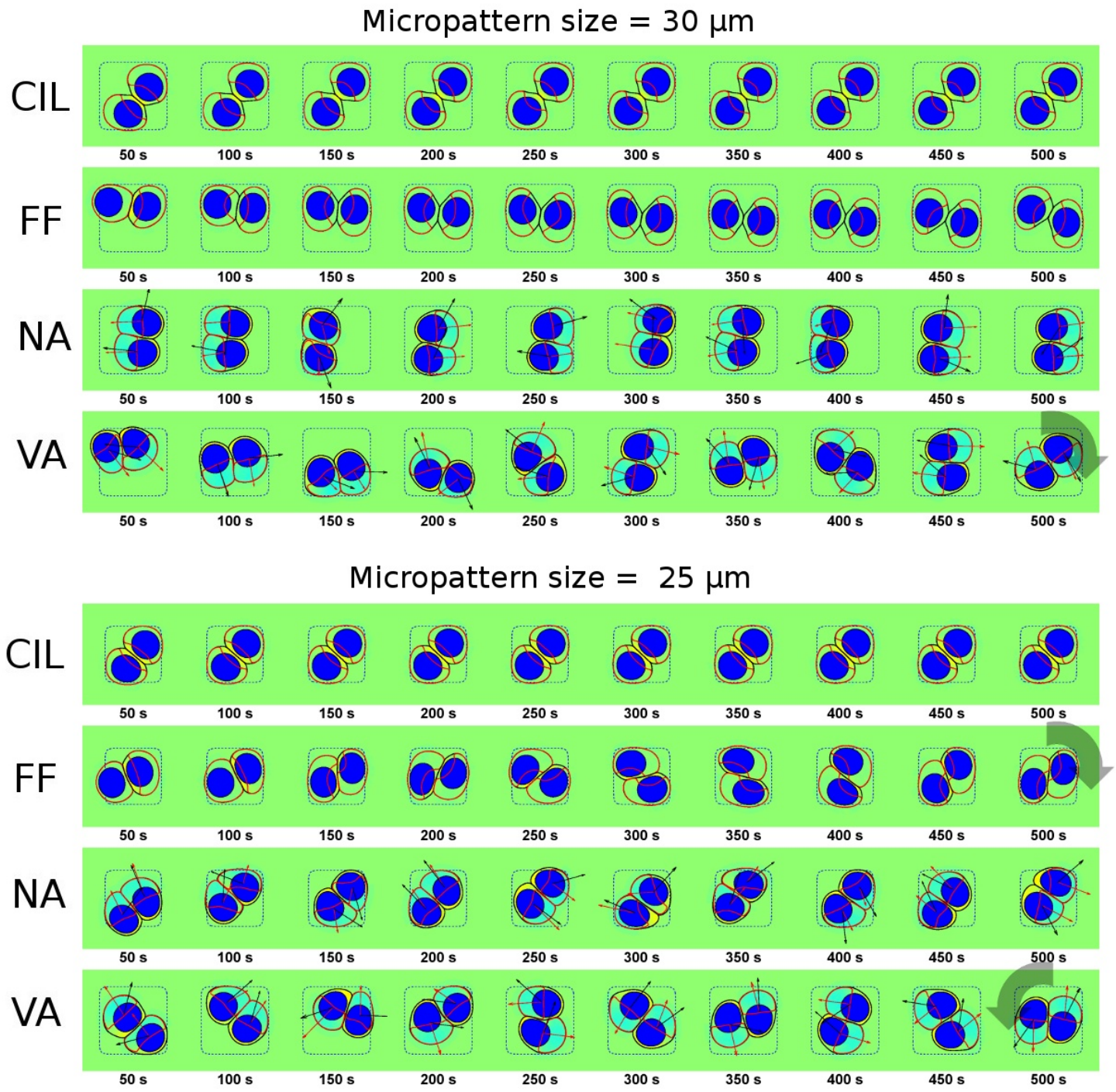

Figure S3: **Polarity mechanisms can control persistent rotational motion, but interacts with micropattern size.** Representative time traces are shown for different polarity mechanisms. TOP: Micropattern size $L_{\text{micro}} = 30\ \mu m$; BOTTOM: Micropattern size $L_{\text{micro}} = 25\ \mu m$ (This figure is repeated from the main text for comparison). See also Supplementary Movies S3-S11.

9 Extensions to different geometries and numbers of cells

It is straightforward to extend our method to different geometries, simply by changing the function $\chi(\mathbf{r})$ that describes the adhesive micropattern. It is in principle also simple to increase the number of cells, though the computational expense increases, and smaller time steps may be required to deal with the added extent of cell-cell adhesion. New, more complex dynamics may also appear when the number of cells increases, including changes in cell contact topology (e.g. as studied in [18]); this will be a focus of future work. We show initial snapshots of two cells and three cells persistently rotating within circular micropatterns as well as three cells rotating within a square micropattern in Fig S5.

10 Nucleus can influence the cell-cell interface shape

We show in Fig. S6 that the nucleus can influence the cell-cell interface's shape, even reversing its chirality. However, this reversal can also be accomplished by varying other parameters.

11 Parameter setting

Our goal in this paper has been to develop a reasonably generic simplified model of mammalian cell motility that can give some insight into the coordination of rotation. However, we are not attempting to fit specific experiments, and so we will use only rough estimates. Where possible, we have chosen to use parameters consistent with our earlier models [1, 5, 19]. The parameters we use by default throughout this paper are given below, in Table S1. We also briefly discuss the justification of these parameters below.

11.1 Cell mechanical parameters

The order of magnitude of the cell tension and bending coefficients was set in [1] by comparison with shear flow experiments on *Dictyostelium* cells [20]. The friction coefficient τ was set by [1] by fitting to experimental data on fish keratocytes [21]. Our cell velocities are chosen to be comparable to keratocyte velocities, $v \sim 0.2\mu m/s$ [21]; this sets the characteristic velocity scale, which is $\alpha\rho^{\text{maximum}}/\tau$; with our reaction-diffusion model, $\rho^{\text{maximum}} \approx 1.4\mu m^{-2}$, so this sets the general scale of $\alpha \approx 0.4pN\ \mu m^{-3}$. β must be chosen so that the highest ρ in the cell is larger than α/β, and the smallest value is lower than α/β. We also found that choosing β too small prevented the nucleus from being effectively pulled by the contraction of the back of the cell.

11.2 Reaction-diffusion parameters

The order of magnitude of the reaction-diffusion parameters was set by comparison to measured Rho GTPase kinetics by [6]; we use the parameters of [19] for the reaction-diffusion mechanism. The dynamics of I are not chosen to model a specific inhibitor, but merely a plausible diffusing molecule generated by various processes. We therefore choose D_I to be of the scale of membrane protein and lipid diffusion coefficients, $D_I = 1\mu m^2/s$ [22]. The degradation rate k_{-I} is at the same timescale as the Rho GTPase kinetics (s^{-1}), and has also been chosen to ensure that cell-cell contacts in the CIL mechanism only generate I near the contact, and not throughout the cell. The noise parameter η is calibrated above.

11.3 Polarity mechanism parameters

Our general approach to the polarity mechanism parameters has been to ensure that the mechanisms strongly determine the cell's polarity, e.g. that in the CIL model, cell-cell contact completely prevents polarity in that direction. We found that choosing $k_I^{\text{CIL,FF}} = 0.25s^{-1}$ was sufficient to do this. For the neighbor-aligning and velocity-aligning cells, $k_I^{\text{NA,VA}} = 0.1s^{-1}$ ensures that the direction of high ρ aligns well with the additional polarity vector $\hat{\mathbf{p}}$. In the NA/VA mechanisms, we choose T_{orient} to be small relative to the timescale of motion (0.02 s compared with tens of seconds for a cell to crawl its own radius), resulting in a polarity that aligns very quickly with its input (either the cell's velocity or the velocity of nearby cells).

11.4 Cell-cell interaction parameters

The cell-cell repulsion parameter g sets the energy for a given area of overlap; we choose it as $1pN/\ \mu m$, or around $250k_BT$ per square micron; this effectively prevents cell-cell overlap. The adhesion scale σ is chosen to be close to the line tension of the cells, ensuring that cells can easily deform to increase their cell-cell contact.

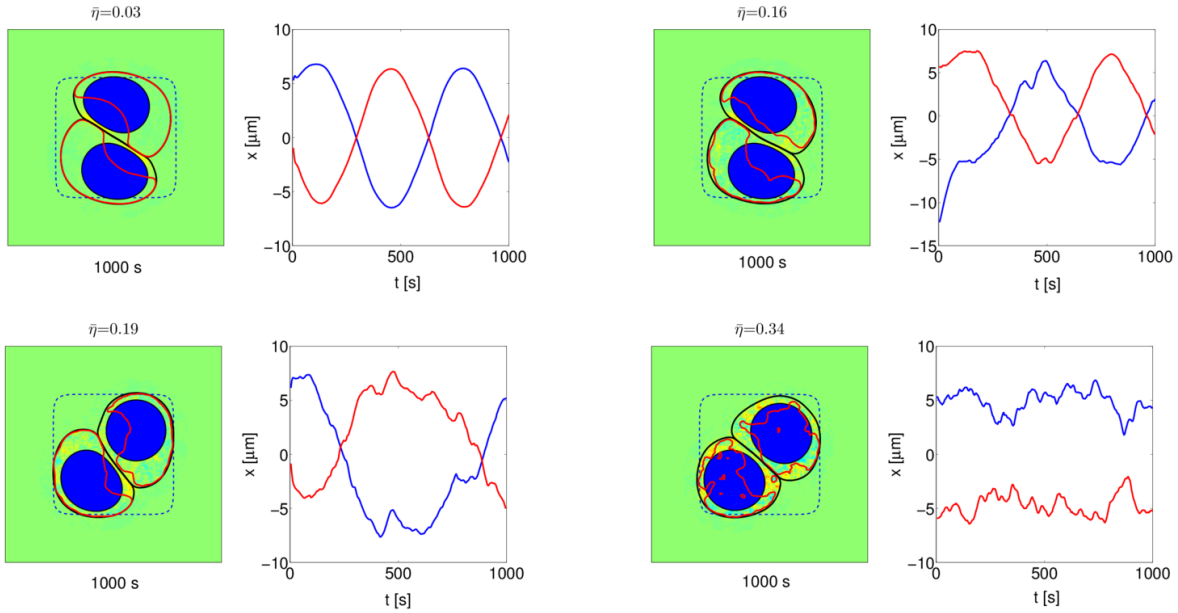

Figure S4: **Decreasing cell persistence disrupts persistent rotational motion.** We show snapshots at 1000 s and traces of each cell's center of mass (projected on the x axis) over time for four different values of the unitless noise of the inhibitor $\bar{\eta}^2 = \eta^2/D_I$. Increasing the noise can cause reversals ($\bar{\eta} = 0.16$) as well as completely suppressing rotation ($\bar{\eta} = 0.34$) These simulations use the FF mechanism and are on a 25-micron adhesive pattern. See also Supplementary Movie S12.

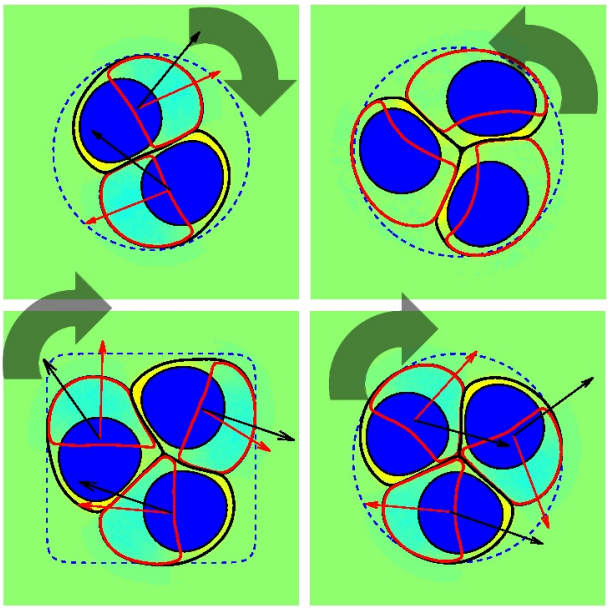

Figure S5: **Our method is simply extended to other patterns and larger numbers of cells.** Here we show snapshots of various extensions to different pattern shapes and larger numbers of cells. These are (upper left) a rotating pair of VA cells on a circular micropattern with diameter $30\mu m$, shown at 1000 s, (upper right) three FF cells on a circular micropattern with diameter $32\mu m$ shown at 1000 s, (lower left) three VA cells on a square micropattern with $L_{\text{micro}} = 32\mu m$ shown at 720 s, and (lower right) three VA cells on a circular micropattern with diameter $32\mu m$ shown at 720 s. Parameters are as given in Table S1, except for the three-cell simulations we have used $\Delta t = 0.0005$ seconds.

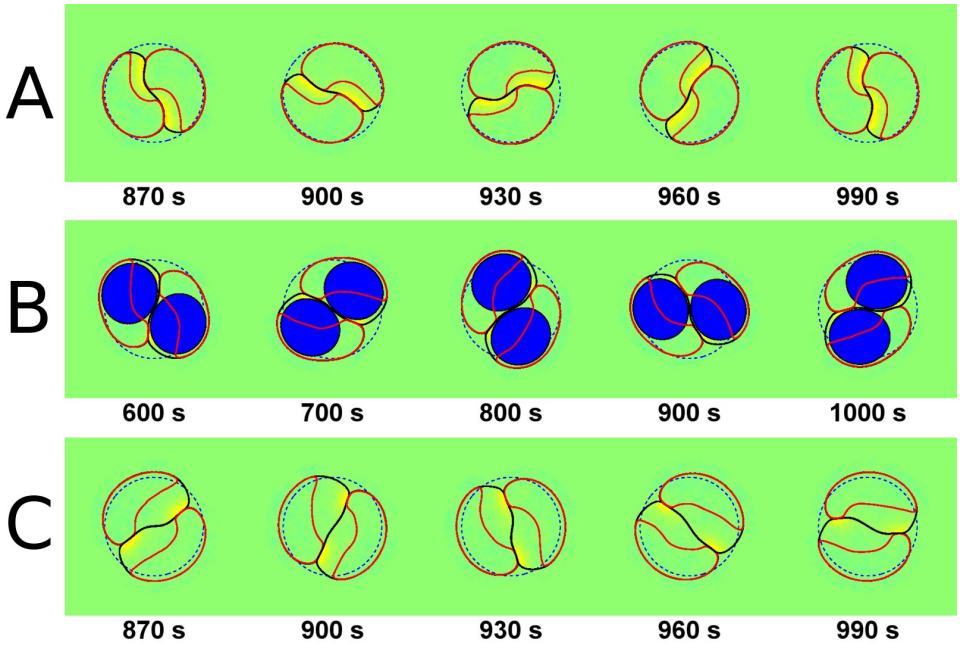

Figure S6: **Nucleus can influence cell-cell interface shape.** We show three time-traces that demonstrate some of the variables contributing to interface shape. We have used a circular micropattern of radius 12.5 μm, and simulate cells with the FF mechanism. A: Cell without a nucleus exhibiting PRM with an interface deformed inward in the back. B: Cell with a nucleus exhibiting PRM with an interface bulging outward at the back. The only difference between A and B is that A has no nucleus. Both A and B have slightly different parameters than our defaults; α is 1.5 times its default value, γ_{nuc} and κ_{nuc} are five times their default value, M is ten times its default value, and the nuclear radius is $7.3\mu m$ ($\Delta t = 0.001s$); these changes are made to highlight the influence of the nucleus. C shows a cell with no nucleus, but with an interface bulging at the back. The cell shown in C has α twice its default value and β half its default value. The interface shapes of B and C are consistent with the experiments of [17], but the shape of A is not.

Table S1: **Table of simulation parameters**

Parameter	Description	Value
α	Protrusion coefficient	0.4 pN / μm^3
β	Retraction coefficient	0.2 pN / μm
γ	Cell tension coefficient	1.8 pN
κ	Cell bending coefficient	1 pN μm^2
g	Cell-cell body repulsion coefficient	1 pN/ μm
σ	Cell-cell adhesion coefficient	1.875 pN/ μm
g_{nuc}	Nucleus confinement coefficient	2 pN/ μm
γ_{nuc}	Nucleus tension coefficient	2 pN
κ_{nuc}	Nucleus bending coefficient	2 pN μm^2
R_{nuc}	Nucleus radius ($A_{\text{nuc}} = \pi R_{\text{nuc}}^2$)	6 μm
R_{cell}	Initial radius of cell	10 μm
M	Nucleus area constraint multiplier	1 pN/ μm^3
τ	Friction coefficient	2.62 pN s / μm^2
τ_{nuc}	Nuclear friction coefficient	1 pN s / μm^2
ϵ	Phase field width	2 μm
k_a	Unitless base activation rate	0.01
k_b	Overall activation rate	10 s^{-1}
k_c	Deactivation rate	10 s^{-1}
K_a	Positive feedback threshold for actin promoter (Rho GTPase) concentration	1 μm^{-2}
D_ρ	Actin promoter (Rho GTPase) diffusion coefficient	0.8 μm^2/s
N_{tot}	Total amount of actin promoter (unitless)	800
D_I	Inhibitor diffusion coefficient	1 μm^2/s
$k_I^{\text{CIL,FF}}$	Rate of I generation from contact inhibition, FF mechanism	0.25 s^{-1}
$k_I^{\text{NA,VA}}$	Rate of I generation from neighbor alignment, velocity alignment	0.1 s^{-1}
k_{-I}	Degradation rate of I	0.2 s^{-1}
T_{orient}	Time scale for polarity orientation in NA and VA models	0.02 s
Δt	Numerical time step	0.002 s
$\bar{\eta}$	Unitless noise strength	0.03
ζ	Alignment noise strength	10 $s^{-1/2}$

These parameters are used throughout the paper; any deviation from them is explicitly noted.

11.5 Nucleus parameters

In modeling the nucleus, we have described it as a phase field with a tension, bending modulus, as well as a constraint ensuring that the area of the nucleus is fixed. M is chosen (much as the similar parameter in [1]) to be large enough that the nuclear area is well-conserved (to around 1%, in a typical simulation). We have chosen the nuclear membrane to have only a slightly higher tension and bending modulus than the cell membrane for computational ease; the largest effect of the nucleus is from its effective incompressibility. τ_{nuc} is set to be slightly smaller than the value τ; we found that significantly larger values of τ_{nuc} could lead to the cell's inability to transport the nucleus. g_{nuc} was set to ensure that the nucleus does not cross the membrane; its value is similar to the cell-cell repulsion.

12 Variation of parameters

In this section, we show that the trends of the regulation of PRM by cell polarity mechanisms are relatively independent of the particular parameters we choose. We vary model parameters, and report the observed phenotype for each polarity mechanism (CIL,FF,VA,NA). These simulations are performed in the 25- μm square micropatterns, and for each model parameter discussed, we run simulations with that parameter multiplied by factors of 0.5, $0.8\bar{3}$, 1.2, and 2. We may adjust the time step for numerical stability; we mark parameter sets with an X where the required time step was too small to reasonably simulate rotation (below 5×10^{-4} s) We find that robustly, 1) CIL cells do not exhibit persistent rotational

motion, 2) VA and FF cells exhibit PRM unless cells become immotile or fail to polarize, except in the case of zero adhesion (discussed below), and 3) NA cells flock unless they become immotile.

In the table below, the following abbreviations are used: P = persistent rotational motion state, F = flocking state, I = immotile state, X = required time step for numerical stability made simulations prohibitively expensive, NRP = not robustly polarized, OC = cells at opposite sides or corners, U = unrealistic (e.g. $R_{\text{nuc}} > R_{\text{cell}}$), O = other.

Table S2: **Parameter variations: FF polarity mechanism in 25 μm micropattern.** (Typical parameters: P)

Parameter	0.5x	$0.8\bar{3}$x	1.2x	2x
γ	P	P	P	NRP,OC (Fig.S7A)
κ	X	P	P	P
α	NRP,OC	P	P	P (Fig.S7B)
β	P	P	P	P
τ	P	P	P	P
g	P	P	P	P
σ	P	P	P	X
k_I	P	P	P	P
k_{-I}	P	P	P	P
D_ρ	P	P	P	P
D_I	P	P	P	P
x_0	P	P	P	P
γ_{nuc}	P	P	P	P
κ_{nuc}	P	P	P	P
g_{nuc}	P	P	P	P
τ_{nuc}	P	P	P	P
M	P	P	P	P
R_{nuc}	P	P	P	U
N_{tot}	I	I	P	NRP,OC
k_a	P	P	P	P
k_b	I	I	P	P
K_a	NRP,OC	P	I	I
k_c	P	P	I	I

Table S3: **Parameter variations: CIL polarity mechanism in 25 μm micropattern**. (Typical parameters: OC)

Parameter	0.5x	$0.8\bar{3}$x	1.2x	2x
γ	OC	OC	OC	OC
κ	X	OC	OC	OC
α	OC	OC	OC	OC
β	OC	OC	OC	OC
τ	OC	OC	OC	OC
g	OC	OC	OC	OC
σ	OC	OC	OC	X
k_I	OC	OC	OC	OC
k_{-I}	OC	OC	OC	OC
x_0	OC	OC	OC	OC
D_ρ	OC	OC	OC	OC
D_I	OC	OC	OC	OC
γ_{nuc}	OC	OC	OC	OC
κ_{nuc}	OC	OC	OC	OC
g_{nuc}	OC	OC	OC	OC
τ_{nuc}	OC	OC	OC	OC
M	OC	OC	OC	OC
R_{nuc}	OC	OC	OC	U
N_{tot}	I	I	OC	NRP,OC
k_a	OC	OC	OC	OC
k_b	I	I	OC	OC
K_a	NRP,OC	OC	I	I
k_c	OC	OC	I	I

Table S4: **Parameter variations: VA polarity mechanism in 25 μm micropattern.** (Typical parameters: P)

Parameter	0.5x	$0.8\bar{3}$x	1.2x	2x
γ	P	P	P	P
κ	X	P	P	P
α	P	P	P	P
β	P	P	P	P
τ	P	P	P	P
g	P	P	P	P
σ	P	P	P	X
k_I	P	P	P	P
k_{-I}	P	P	P	P
D_ρ	P	P	P	P
D_I	P	P	P	P
γ_{nuc}	P	P	P	P
κ_{nuc}	P	P	P	P
g_{nuc}	P	P	P	P
τ_{nuc}	P	P	P	P
M	P	P	P	P
R_{nuc}	P	P	P	U
N_{tot}	I	P	P	P
k_a	P	P	P	P
k_b	I	P	P	P
K_a	P	P	P	I
k_c	P	P	P	I

Table S5: **Parameter variations: NA polarity mechanism in 25 μm micropattern.** (Typical parameters: F)

Parameter	0.5x	0.83x	1.2x	2x
γ	F	F	F	F
κ	X	F	F	F
α	F	F	F	F
β	F	F	F	F
τ	F	F	F	F
g	F	F	F	F
σ	F	F	F	X
k_I	F	F	F	F
k_{-I}	F	F	F	F
D_ρ	F	F	F	F
D_I	F	F	F	F
γ_{nuc}	F	F	F	F
κ_{nuc}	F	F	F	F
g_{nuc}	F	F	F	F
τ_{nuc}	F	F	F	F
M	F	F	F	F
R_{nuc}	F	F	F	U
N_{tot}	I	F	F	F
k_a	F	F	F	F
k_b	I	F	F	F
K_a	F	F	F	I
k_c	F	F	F	I

There are several trends worth noting in these tables. The most obvious one is that most parameters are irrelevant to the presence or absence of collective motion, though they may change the morphology of the cells. In particular, none of the nuclear parameters affect the qualitative motility behavior, and neither do the diffusion coefficients $D_{I,\rho}$, or the parameters related to the strength of the polarity interaction (k_I, k_{-I}, x_0). However, effects that either prevent single cells from polarizing or create large deformations in single-cell shape can inhibit motility. For instance, we note that the ability of the cell to polarize in the FF and CIL models is strongly dependent on the total amount of Rho GTPase, $N_{\rm tot}$ - if $N_{\rm tot}$ is too small (large), ρ becomes homogeneous and small (large). This is well-understood as a feature of the reaction-diffusion mechanism [5,6,23]. This effect is somewhat weaker in the NA and VA models, because we bias the ρ dynamics to align with our auxiliary polarity variable $\hat{\mathbf{p}}$. Similarly, the ability to polarize depends systematically on the reaction-diffusion parameters for the ρ model, k_a, k_b, K_a, k_c. Mechanical parameters may also play a role in prohibiting motility: if α is too small (weak protrusion) or γ is too large (high tension), cells may not be able to effectively protrude (see, e.g. Fig.S7A). The central point we make here is that the distinction between FF, CIL, VA, and NA is reasonably robust, and deviations from what we present in the main paper are mostly at parameters where cells are not even motile - unrealistic models for the experiments of Huang et al. [17].

Numerical instability is an issue in two specific cases: large σ and small κ. In our phase-field equations for ϕ, we have two terms that are fourth order in gradients: one proportional to κ, derived from membrane bending, which is handled implicitly, and one from cell-cell adhesion, proportional to σ, handled explicitly (see Section 13). When the explicitly-handled term dominates, we have numerical difficulties; these may be resolved by increasing κ. In the cases of large σ and small κ, we have not been able to choose a high enough time step to robustly identify behavior. In addition, in these cases, we see lattice artifacts where cell-cell interfaces prefer to align along particular orientations in space.

We point out a few interesting cases in Fig.S7 which are also noted in the table above. In case A, the tension γ is increased by a factor of two in the FF model, leading to effectively circular cells. In this case, no PRM is created, and only one cell at a time is polarized; this oscillates sporadically. In B, the protrusion strength α is increased by a factor of two in the FF model. This is a case where the morphology of the cell-cell pair appears different - with a larger spread area. This may more closely correspond to the experiments of Huang et al. [17]. We also show in Fig.S7C a case without adhesion ($\sigma = 0$); NA, CIL, and VA maintain their phenotypes (though CIL cells do not remain in contact), but the FF mechanism requires persistent cell-cell contact to drive PRM, and PRM is absent if there is no adhesion.

From these parameter variation studies, we argue that the distinctions between CIL, FF, NA, and VA polarity mechanisms are robust, and that the parameters presented in the main paper are reasonably representative. This suggests that the fundamental nature of the polarity mechanism qualitatively regulates the existence of PRM.

13 Numerical details

We describe briefly some of the important details in our numerical solution of these equations. We will mostly discuss these in the single-cell case; the multi-cell case is a simple generalization.

We solve the phase field equation in a semi-implicit spectral fashion (e.g. [24]), handling the high-order derivatives from the single-cell bending and tension terms implicitly, but all other terms explicitly. For a single cell, the phase field equation is (expanding the functional derivative),

$$\partial_t \phi(\mathbf{r},t) = \frac{1}{\tau}\left[\alpha\chi(\mathbf{r})\rho(\mathbf{r}) - \beta\right]|\nabla\phi| + \frac{\gamma}{\tau}\left[\nabla^2\phi - \frac{G'(\phi)}{\epsilon^2}\right] - \frac{\kappa}{\tau}\left[\nabla^2 - \frac{G''(\phi)}{\epsilon^2}\right]\left[\nabla^2\phi - \frac{G'(\phi)}{\epsilon^2}\right]. \tag{S24}$$

We define the explicitly-handled part of this equation as

$$F_{\rm exp}(t) = \frac{1}{\tau}\left[\alpha\chi(\mathbf{r})\rho(\mathbf{r}) - \beta\right]|\nabla\phi| - \frac{\gamma}{\tau}\frac{G'(\phi)}{\epsilon^2} + \frac{\kappa}{\tau}\nabla^2\left[\frac{G'(\phi)}{\epsilon^2}\right] + \frac{\kappa}{\tau}\frac{G''(\phi)}{\epsilon^2}\left[\nabla^2\phi - \frac{G'(\phi)}{\epsilon^2}\right]. \tag{S25}$$

We then can write the semi-implicit form

$$\phi(\mathbf{r},t+\Delta t) - \frac{\Delta t\gamma}{\tau}\nabla^2\phi(\mathbf{r},t+\Delta t) + \frac{\Delta t\kappa}{\tau}\nabla^4\phi(\mathbf{r},t+\Delta t) = \phi(\mathbf{r},t) + \Delta t\; F_{\rm exp}(t) \tag{S26}$$

which can be easily solved by Fourier transforming:

$$\phi(\mathbf{q},t+\Delta t) = \frac{\phi(\mathbf{q},t) + \Delta t\;\left\{F_{\rm exp}(t)\right\}_{\mathbf{q}}}{1 + (\Delta t\gamma/\tau)\,q^2 + (\Delta t\kappa/\tau)\,q^4} \tag{S27}$$

where $\{\cdots\}_{\mathbf{q}}$ indicates a Fourier transform. We move between real and Fourier space using the Fast Fourier Transform. In the multi-cell case, we handle all adhesion terms explicitly.

We solve the reaction-diffusion equations explicitly, using the same time-stepping algorithm presented in [5], but with one modification for the presence of stochastic noise. To solve the stochastic differential equation for $I(\mathbf{r})$, we use a simple Euler-Maruyama method [25] combined with the stepping used in [5]:

$$I(t+\Delta t) = \frac{2\phi(t) - \phi(t+\Delta t)}{\phi(t)}I(t) + \Delta t\frac{\nabla\cdot\left[\phi(t)D_I\nabla I(t)\right]}{\phi(t)} + \Delta t f_{I,\rm deterministic}\left[I(t),\{\phi(t)\},\cdots\right] + \Xi(\mathbf{r},\Delta t). \tag{S28}$$

We only divide by $\phi(t)$ in the region where $\phi(t) \geq \lambda$, where $\lambda = 10^{-4}$. Outside of this region, we set $I(t+\Delta t) = I(t)\phi(t)$. Here, $\Xi(\mathbf{r}, \Delta t) = \int_t^{t+\Delta t} dt' \xi(\mathbf{r}, t')$ is a Gaussian random variable with zero mean and variance $\langle \Xi(\mathbf{r}, \Delta t)\Xi(\mathbf{r}', \Delta t)\rangle = \eta^2 \Delta t \delta(\mathbf{r} - \mathbf{r}')$; here $\delta(\mathbf{r})$ is the Dirac delta function. We want to represent this delta function, which is continuous, on our grid. To do this, we need to ensure that our representation maintains the normalization of the Dirac delta function $\int d^2 r \delta(\mathbf{r}) = 1$. On a square lattice with spacing Δx, this would be $\int d^2 r \delta(r) \rightarrow \sum_{\text{sites } \mathbf{r}} \Delta x^2 \tilde{\delta}_{\mathbf{r}} = 1$. This suggests that we choose $\tilde{\delta}_{\mathbf{r}}$ as the Kronecker delta divided by Δx^2, i.e. $\tilde{\delta}_{\mathbf{r}} = \Delta x^{-2}\, \delta_{\mathbf{r},\mathbf{0}}$. We therefore choose our noise $\Xi(\mathbf{r}, \Delta t)$ to be uncorrelated between lattice sites, with each grid point having a variance of $\eta^2 \Delta t \Delta x^{-2}$. The ρ equation is solved with the same stepping described in Eq.S28, though without a stochastic term.

We also do not solve the phase field equation and reaction-diffusion equations in the entire domain; we only solve these equations in a box near each cell. This box is recentered if the cell is close to the boundary of this box: if $\phi \geq 0.5$ within ten pixels of the boundary, the box is shifted 20 pixels. (The new pixels at the edge of the box are created either as zero (for ρ, I, ν) or by a periodic shift (ϕ); we expect these details far away from the cell to be irrelevant.) The small box surrounding each cell is 50 $\mu m \times 50$ μm (128×128 points). We treat the small box as having periodic boundary conditions, which is appropriate as we keep the cell from too closely approaching the edge. The whole system is 100 $\mu m \times 100$ μm (256×256). To construct terms such as $\sum \phi_j$, which involve sums over many individual fields, we assume that each $\phi_i = 0$ outside of the box it is defined in. This technique will allow us to increase the size of the system and the number of cells studied in the future.

References

[1] Danying Shao, Wouter-Jan Rappel, and Herbert Levine. Computational model for cell morphodynamics. Physical Review Letters, 105(10):108104, 2010.

[2] Anne-Florence Bitbol and Jean-Baptiste Fournier. Forces exerted by a correlated fluid on embedded inclusions. Physical Review E, 83(6):061107, 2011.

[3] Pierre C Hohenberg and Bertrand I Halperin. Theory of dynamic critical phenomena. Reviews of Modern Physics, 49 (3):435, 1977.

[4] Charles W Wolgemuth, Jelena Stajic, and Alex Mogilner. Redundant mechanisms for stable cell locomotion revealed by minimal models. Biophysical Journal, 101(3):545–553, 2011.

[5] Brian A Camley, Yanxiang Zhao, Bo Li, Herbert Levine, and Wouter-Jan Rappel. Periodic migration in a physical model of cells on micropatterns. Physical Review Letters, 111(15):158102, 2013.

[6] Y. Mori, A. Jilkine, and L. Edelstein-Keshet. Wave-pinning and cell polarity from a bistable reaction-diffusion system. Biophysical Journal, 94(9):3684, 2008.

[7] Gillian L Ryan, Naoki Watanabe, and Dimitrios Vavylonis. A review of models of fluctuating protrusion and retraction patterns at the leading edge of motile cells. Cytoskeleton, 69(4):195, 2012.

[8] Jun Allard and Alex Mogilner. Traveling waves in actin dynamics and cell motility. Current Opinion in Cell Biology, 25, 2013.

[9] Changji Shi, Chuan-Hsiang Huang, Peter N Devreotes, and Pablo A Iglesias. Interaction of motility, directional sensing, and polarity modules recreates the behaviors of chemotaxing cells. PLoS Computational Biology, 9(7):e1003122, 2013.

[10] Alain Karma and Wouter-Jan Rappel. Quantitative phase-field modeling of dendritic growth in two and three dimensions. Physical Review E, 57(4):4323, 1998.

[11] Makiko Nonomura. Study on multicellular systems using a phase field model. PloS ONE, 7(4):e33501, 2012.

[12] Balint Szabo, GJ Szöllösi, B Gönci, Zs Jurányi, David Selmeczi, and Tamás Vicsek. Phase transition in the collective migration of tissue cells: experiment and model. Physical Review E, 74(6):061908, 2006.

[13] Markus Basan, Jens Elgeti, Edouard Hannezo, Wouter-Jan Rappel, and Herbert Levine. Alignment of cellular motility forces with tissue flow as a mechanism for efficient wound healing. Proceedings of the National Academy of Sciences, 110(7):2452, 2013.

[14] Brian A Camley and Wouter-Jan Rappel. Velocity alignment leads to high persistence in confined cells. Physical Review E, 89:062705, 2014.

[15] Silke Henkes, Yaouen Fily, and M Cristina Marchetti. Active jamming: self-propelled soft particles at high density. Physical Review E, 84(4):040301, 2011.

[16] Tamás Vicsek, András Czirók, Eshel Ben-Jacob, Inon Cohen, and Ofer Shochet. Novel type of phase transition in a system of self-driven particles. Physical Review Letters, 75(6):1226, 1995.

[17] S Huang, CP Brangwynne, KK Parker, and DE Ingber. Symmetry-breaking in mammalian cell cohort migration during tissue pattern formation: role of random-walk persistence. Cell Motility and the Cytoskeleton, 61(4):201, 2005.

[18] Dapeng Bi, Jorge H Lopez, JM Schwarz, and M Lisa Manning. Energy barriers and cell migration in densely packed tissues. Soft Matter, 10(12):1885, 2014.

[19] D. Shao, H. Levine, and W.-J. Rappel. Coupling actin flow, adhesion, and morphology in a computational cell motility model. Proceedings of the National Academy of Sciences, 109(18):6851, 2012.

[20] Rudolf Simson, Eva Wallraff, Jan Faix, Jens Niewöhner, Günther Gerisch, and Erich Sackmann. Membrane bending modulus and adhesion energy of wild-type and mutant cells of dictyostelium lacking talin or cortexillins. Biophysical Journal, 74(1):514, 1998.

[21] Kinneret Keren, Zachary Pincus, Greg M Allen, Erin L Barnhart, Gerard Marriott, Alex Mogilner, and Julie A Theriot. Mechanism of shape determination in motile cells. Nature, 453(7194):475, 2008.

[22] Marten Postma, Leonard Bosgraaf, Harriët M Loovers, and Peter JM Van Haastert. Chemotaxis: signalling modules join hands at front and tail. EMBO Reports, 5(1):35, 2004.

[23] Y. Mori, A. Jilkine, and L. Edelstein-Keshet. Asymptotic and bifurcation analysis of wave-pinning in a reaction-diffusion model for cell polarization. SIAM Journal on Applied Mathematics, 71(4):1401, 2011.

[24] LQ Chen and Jie Shen. Applications of semi-implicit fourier-spectral method to phase field equations. Computer Physics Communications, 108(2):147, 1998.

[25] Peter E Kloeden and Eckhard Platen. Numerical solution of stochastic differential equations, volume 23. Springer, 1992.

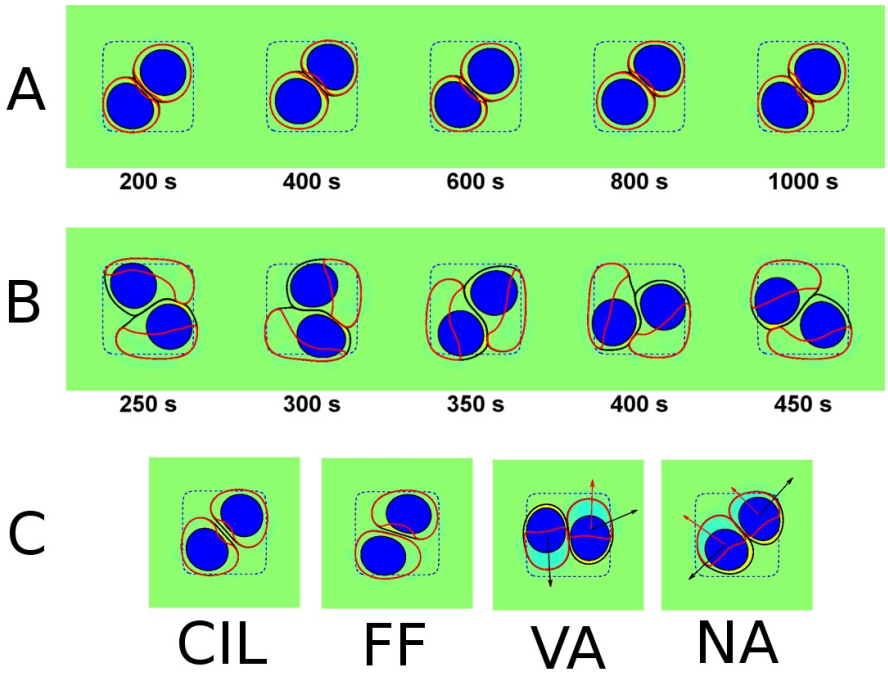

Figure S7: **Interesting phenotypes arising from parameter variations.** These simulations are (A) FF with γ twice its default value, (B) FF with α twice its default value. In (C) we set $\sigma = 0$, i.e. completely turn off adhesion and show snapshots at 1000 seconds for CIL, FF, VA, and NA. Parameters not specified are as in Table S1, with $L_{\text{micro}} = 25\mu m$.